Research Article

Universal and stable medical image generation for tissue segmentation (The unistable method)

Ihab ELAFF[1,*], Ali EL-KEMANY[2], Mohamed KHOLIF[3]

[1]Department of Computer Engineering, Faculty of Engineering and Natural Sciences, Üsküdar University,
İstanbul, Turkey
[2]Department of Computer Engineering, College of Engineering & Technology, Arab Academy for Science,
Technology, & Maritime Transport, Alexandria, Egypt
[3]Department of Information Systems, College of Computing & Information Technology,
Arab Academy for Science, Technology, & Maritime Transport, Alexandria, Egypt

Abstract: Segmentation of medical images has been one of the most important research areas because of its impact in modeling and diagnosing the structure and the functions of various organs. The lack of unique solution for the segmentation problem of medical images is caused by the wide range of selections among different medical imaging modalities and clustering methods where each setting has its own estimates for solving this problem. The unistable method is a novel method that generates enhanced images with high contrast, which can reduce boundary overlap between different tissues. This is accomplished by fusion of different clustering maps, which are generated from selected medical images using some clustering methods. The improved unistable images are somehow universal, where all estimates of different regular segmentation settings are considered in the solution, and they are relatively stable, because results of their segmentation are proved to be relatively independent of clustering method.

Key words: Unistable method, unistable image, brain, diffusion tensor imaging, segmentation, white matter, gray matter, cerebrospinal fluid

1. Introduction

Segmentation of medical images has been one of the most important research areas for several years because of its important impact on modeling and diagnosing the structure and the function of different organs. Precise tissue segmentation serves in various medical applications such as radiotherapy planning, image-guided interventions, surgical planning, and evaluation of tissue disorders caused by tumors or Alzheimer disease. It is only possible to obtain macroscale images because of scanners' limited resolution, where each sample represents the average property of the corresponding group of tissues for each zone [1,2]. This limitation is the main reason for the boundary-overlap problem between neighboring tissues in medical images [3–5], and, as a result, automatic medical image segmentation is difficult to be achieved; therefore, simple segmentation methods such as manual thresholds are still in use. Selection of suitable threshold values to separate different tissues in medical images is still a challenge where a range of values is suggested within the same medical imaging modality and for the same group of tissues [6–9]. Tissues of living beings in any part of the body are assumed to be almost uniform [10]. In medical images, such as magnetic resonance imaging (MRI) [11] and computed tomography scans [12], similar

---

*Correspondence: ihab_el_aff@hotmail.com

tissues appear as areas of almost the same grayscale. Segmentation methods are classified into 3 types: region-based methods, boundary-based methods, and hybrid methods, of which region-based methods are widely used in medical image segmentation [2,4,5,13–19]. Region-based segmentation rely are used on clustering methods such as Otsu [20], K-means [21], expectation maximization (EM) [22], C-means and fuzzy C-means (FCM) [23], Markov random field, and iterated conditional modes (ICM) [4,5,18,19]. It should be taken into consideration that there is no unique solution for the segmentation problem where different results are produced by changing the clustering method and/or the selected numbers of clusters [2,4,5,13,14,16,19,23–27]. The human brain is taken as a case study for this research. The brain is composed of three main components: white matter (WM), gray matter (GM), and cerebrospinal fluid (CSF). GM represents almost 50% of the whole brain volume, WM represents almost 37% of the whole brain volume, and CSF represents almost 13% of the whole brain volume [28,29]. CSF contains the largest amount of water among these three components. Arrangement of water particles for each of these components differs as water particles of CSF are completely free; however, water contents of WM are arranged in a very restricted order inside the myelinated axons, and for GM water particles are arranged in axons but not very restricted as in WM. In other words, the CSF is isotropic material with larger amounts of water particles, GM is anisotropic material with relatively low amounts of water, and finally WM is highly anisotropic material with relatively the lowest amount of water.

Wen et al. [23] proposed an improved FCM algorithm with spatial constraints that could effectively segment images that are corrupted by noise, outliers, and other imaging artifacts. They tested FCM, self-organization maps, and FCM with spatial constraints (SFCM) on diffusion tensor imaging (DTI) data (synthetic and real) and compared the results to multichannel and multispectral fusion. El-Aff [14] performed a comparative study on 3 clustering methods, Otsu, K-means, and ICM, to segment brain components based on DTI data. It was shown in this study that the diffusion volume (DV) scalar index produces improved results for CSF/non-CSF segmentation. The obtained rates of CSF, WM, and GM in the final clustering maps were almost 18%, 34%, and 48%, respectively. Portela et al. [13] proposed a semisupervised clustering technique for MRI data composed of two modules. First a random selected slice was clustered by the K-means algorithm, and then each cluster was labeled by an expert and their statistical parameters were computed. Secondly, tissue classes' parameter values were used as initial parameters for a Gaussian mixture model to cluster the remaining slices. The obtained rates of CSF, WM, and GM in the final clustering maps were 18.4%, 35.2%, and 46.4%, respectively. Zhang et al. [16] presented a method based on hidden Markov random field (HMRF) and the associated Markov random field map estimation and the EM fitting procedures. A bias field correction algorithm was used as a presegmentation step for MRI data to avoid wrong initial parameter estimation through intensity normalization. Freitas et al. [24] proposed an approach for segmentation of the midsagittal section of the corpus callosum using the watershed transform. The results were compared with manual segmentation. A method for 3D volume segmentation was also proposed in this research paper. Song et al. [25] presented a method of information integration in a graph-based framework. In addition to image intensity, tissue priors and local boundary information were integrated into the edge weight metrics in the graph. Furthermore, inhomogeneity correction was incorporated by adaptively adjusting the edge weights according to the intermediate inhomogeneity estimation. The results were compared with a segmentation method based on ICM. Awate et al. [26] proposed a segmentation strategy based on a Markov statistical image model that learns automatically from the input data. It formulates the segmentation problem as an optimization problem to maximize the dependency or mutual information between the segmentation labels and the Markov image statistics. Li et al. [2,27] presented a method for automatic brain segmentation based on the multichannel fusion of DTI data.

The segmentation process uses the EM algorithm in combination with the HMRF model. The obtained results from that study were 21.4% CSF and 49.5% WM. This research aims to develop a new method (the unistable method) that generates enhanced images with high contrast and reduced boundary overlap between different tissues.

2. Materials and methods

2.1. Diffusion tensor imaging

DTI is an MRI technique that enables the measurement of the restricted diffusion of water particles in tissue [1]. DTI produces data that describe tissues fibers in terms of eigenvalues and eigenvectors. For medical applications and diagnosing therapies, DTI data are usually described as grayscale images in terms of rotational invariant quantities or scalar indices (SIs) such as mean diffusivity (MD), fractional anisotropy (FA), rational anisotropy (RA), linear anisotropy (Cl), spherical anisotropy (Cs), volume ratio (VR), angular anisotropy (AA), and DV [1–3,30–33]. Datasets of this study were acquired from the Johns Hopkins Medical Institute website. These datasets consist of brains' DTI volume data. Each brain DTI volume contains 50 slices of 256×256 voxels per slice. Each dataset has a file that contains 35 gradient orientations, which are used to calculate tensor data. In every slice, voxel width = 0.9375 mm, voxel height = 0.9375 mm, and space between two successive slices = 2.5 mm.

2.2. The unistable method

The lack of unique solution for solving medical image segmentation problems is caused by the wide range of selections among different medical imaging modalities and clustering methods where each setting has its own estimate. The unistable method is developed to generate enhanced images with high contrast where boundary overlap between different tissues is reduced. The generated unistable images are somehow universal, where all estimates of different regular segmentation settings are considered in the solution, and they are relatively stable, because results of their segmentation are relatively independent of clustering method. This makes the segmentation process of medical images reduced from selection among many medical imaging modalities and many clustering methods, to become selection using only one unistable image and any clustering method. For $\boldsymbol{N}$ images, which contain clear features about the required tissues, $\boldsymbol{M}$ clustering methods with $\boldsymbol{L}$ different settings generate $\boldsymbol{N} \times \boldsymbol{M} \times \boldsymbol{L}$ estimates of normalized clustering maps (CMs). Unistable image IMG_{Uni} is generated by fusing the functions of these CMs together, where:

$$IMG_{Uni.} = \sum_{i=0}^{NxMxL-1} F(CM_i) \tag{1}$$

In this study the unistable method is applied to brain DTI SIs to distinguish between CSF and non-CSF tissues and again to distinguish between WM and non-WM tissues. In both cases, four clustering methods are used to generate CMs, namely Otsu, K-means, FCM, and SFCM. The generic setting for the unistable method is chosen by using only CMs, which provides estimates of 3 clusters, namely tissue, nontissue, and background.

2.3. CSF/non-CSF unistable image generation

Five SIs are used to generate CSF/non-CFS unistable images (CSF_{Uni}), where CSF appears in these images as light regions, and they are DV, MD, $\lambda 1$, $\lambda 2$, and $\lambda 3$ (Figure 1). With four clustering methods (Otsu, K-means,

FCM, and SFCM), 20 CMs are produced. The generic CSF $_{Uni}$ is generated by finding the sum of all of these CMs (Figure 2), and then:
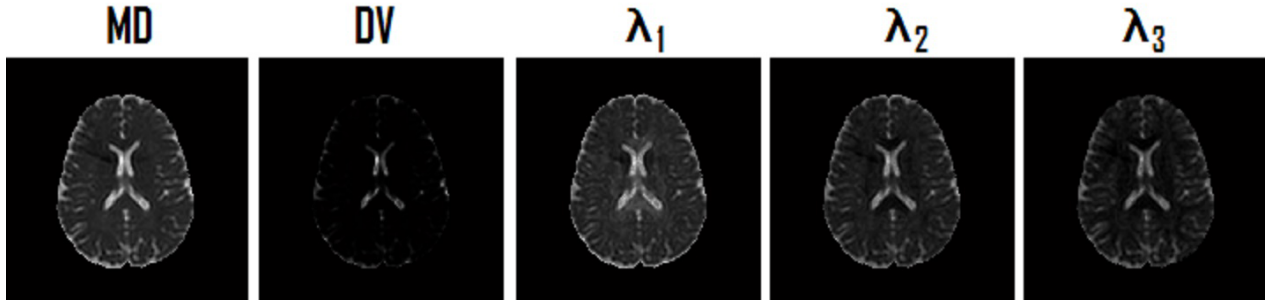

Figure 1. The five scalar indices (DV, MD, λ_1, λ_2, and λ_3) used to generate CSF/non-CSF unistable images.
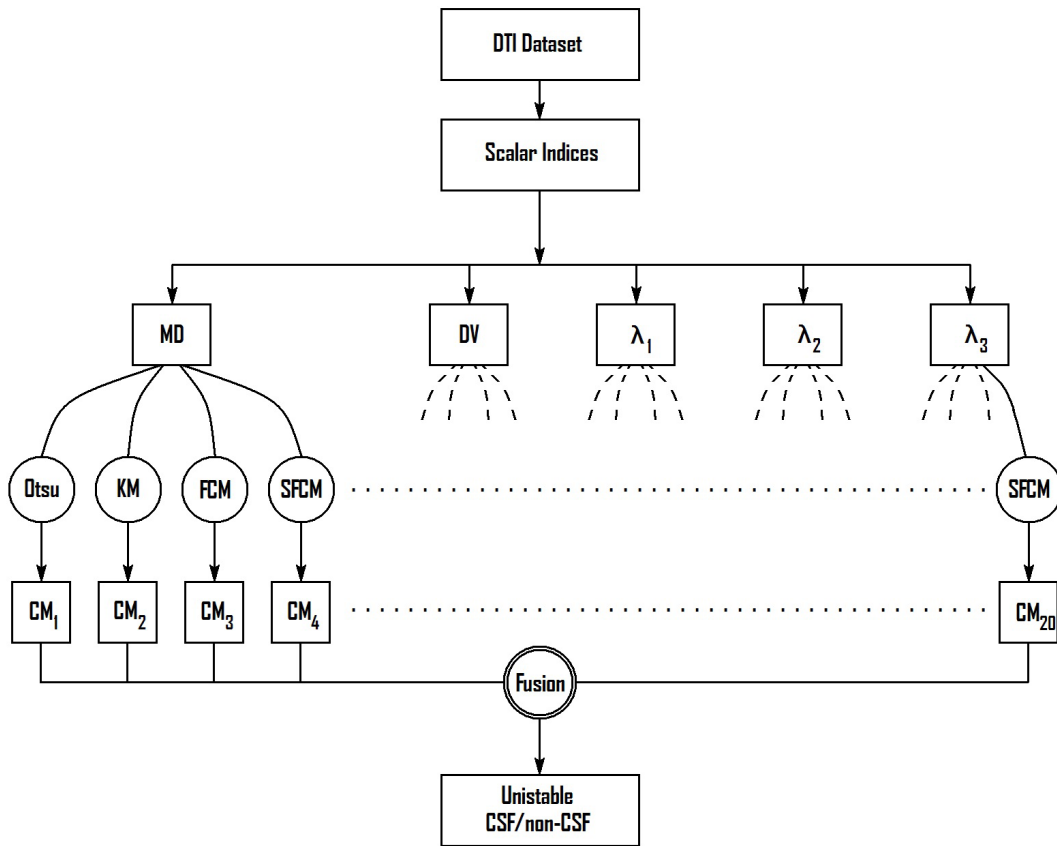

Figure 2. CSF/non-CSF unistable image generation block diagram.

$$F(CM_i) = CM_i \tag{2}$$

Then:

$$CSF_{Uni} = \sum_{i=0}^{NxMxL-1} CM_i \tag{3}$$

As shown in Figure 3, the generic CSF_{Uni} has higher contrast compared to the regularly used MD scalar index. More justification for the obtained results' improvements will be stated in the next section.
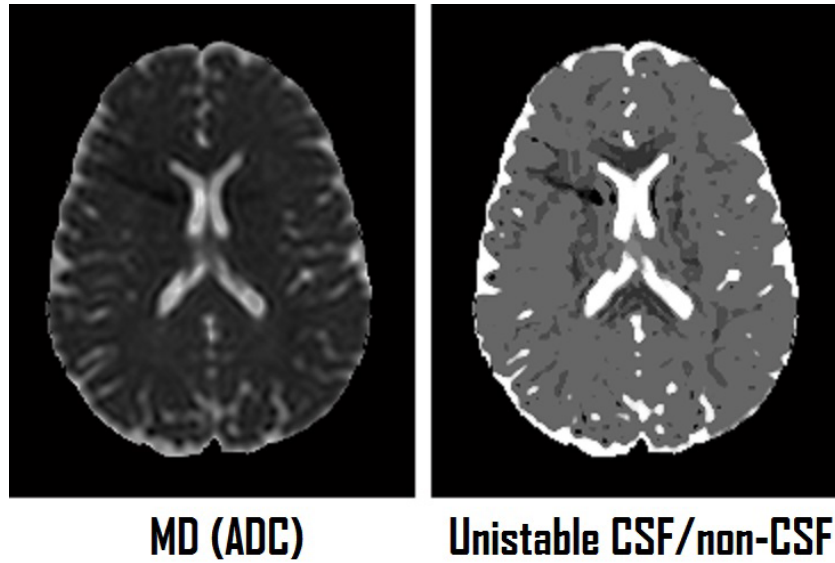

Figure 3. MD image compared to CSF/non-CSF unistable image with generic settings.

2.4. WM and non-WM unistable image generation

Five SIs are used to generate WM/non-WM unistable images (WM_{Uni}), and they are FA, RA, VR, AA, and Cl (Figure 4), where WM appears in these images as light regions except for VR, where WM appears as dark regions. With four clustering methods (Otsu, K-means, FCM, and SFCM), 20 CMs are produced. The generic WM_{Uni} is generated by the following equations (Figure 5):
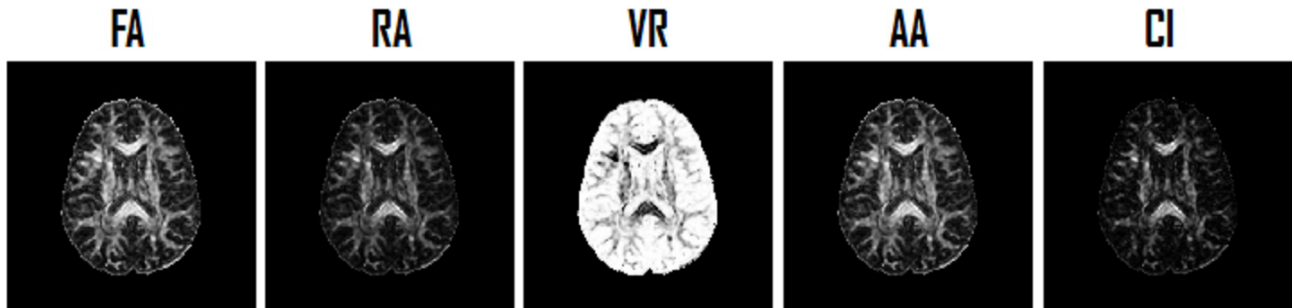

Figure 4. The five scalar indices (FA, RA, VR, AA, and C_l) used to generate WM/non-WM unistable images.

$$F(CM_i) = \begin{cases} 1 - CM_i & \text{for} \quad VR \, \forall \, CM_i(x,y) \neq 0 \\ CM_i & \text{else} \end{cases} \tag{4}$$

Here $CM_i(x,y) \neq 0$ means a nonbackground point, which makes:

$$WM_{Uni} = \sum_{i=0}^{NxMxL-1} F(CM_i) \tag{5}$$

As shown in Figure 6, the generic WM_{Uni} has higher contrast compared to the regularly used FA scalar index. More justification for the obtained results' improvements will be stated in the next section.
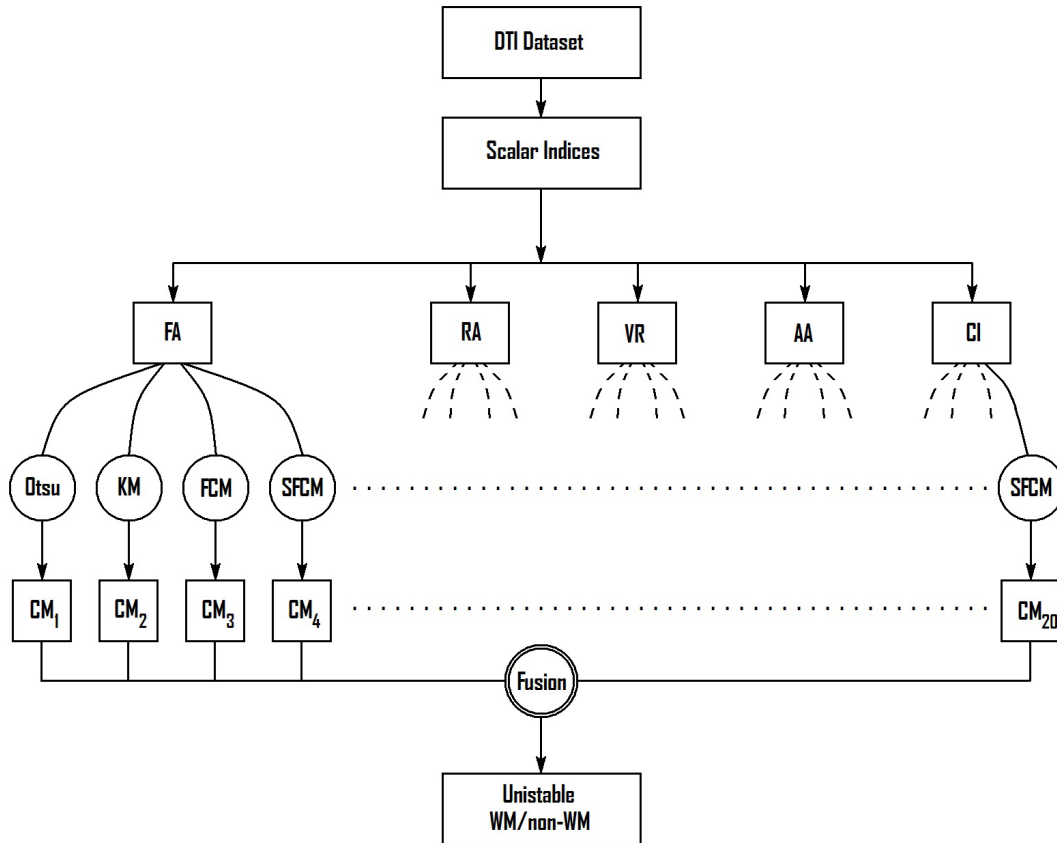

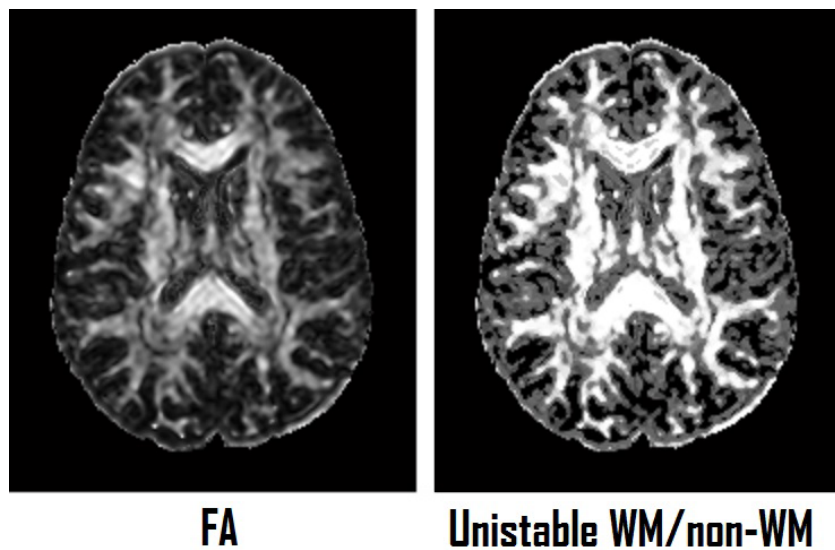**Figure 5.** WM/non-WM unistable image generation block diagram.

Figure 6. FA image compared to WM/non-WM unistable image with generic settings.

3. Results

The stability of the generated unstable images is measured using the rotation estimation (RE) technique (also called cross-validation) [34]. The RE technique is one of the most commonly used models for evaluating the results of statistical analysis that are generalized to an independent dataset. This technique is used to evaluate the stability of the produced unstable images and other images against different clustering methods. The unstable method has been applied to 5 different human brains to generate both CSF_{Uni} and WM_{Uni}. The average mean and the average standard deviation of the obtained RE results for these brains (RE_{AVG}) show that CSF_{Uni} and WM_{Uni} produce the lowest values compared to other images, which means they are closer to being independent of the clustering algorithm (Tables 1 and 2). It was reported that thresholds of normalized MD images with values around 0.3 can efficiently separate the images into CSF/non-CSF clustering maps [7]. Furthermore, thresholds of normalized FA images with values between 0.25 and 0.45 can separate images into WM/non-WM clustering maps [35]. By finding the maximum match (minimum difference) between clustering maps generated by using a range of thresholds around these values and different cluster maps of the selected SIs and unstable images generated by clustering algorithms, the unstable results point to similar threshold levels, but other SIs have a range of values (Figures 7 and 8). For 5 brains, the mean value of the maximum match threshold using 4 different clustering methods is within the range of normal values and the SD value of the maximum match threshold is the smallest among other SIs. This also proves that unstable images are closer to being clustering algorithm-independent (Tables 3 and 4).
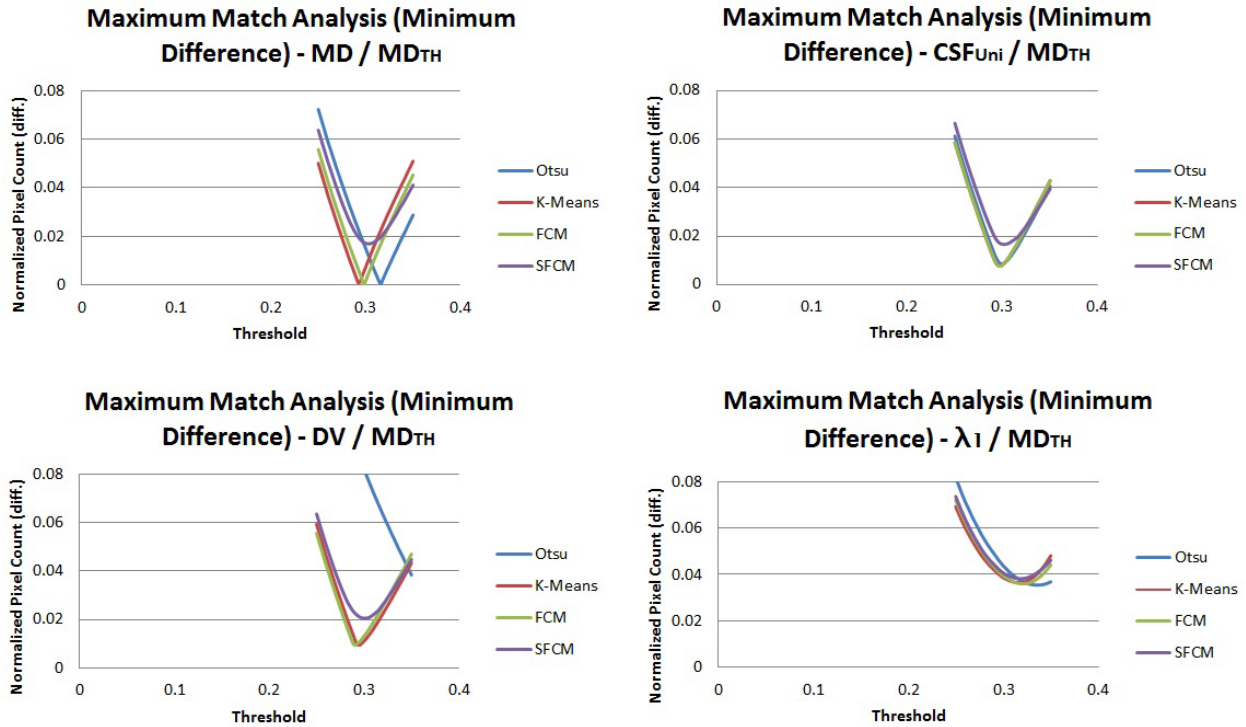

Figure 7. Maximum match analysis for CSF segmentation using MD threshold clustering maps and some cluster maps generated using some clustering methods for different images.

4. Discussion and conclusion

The unstable method is a novel technique for medical image enhancement that produces unstable images of high contrast and reduced boundary overlap among different tissues. The unstable images are somehow
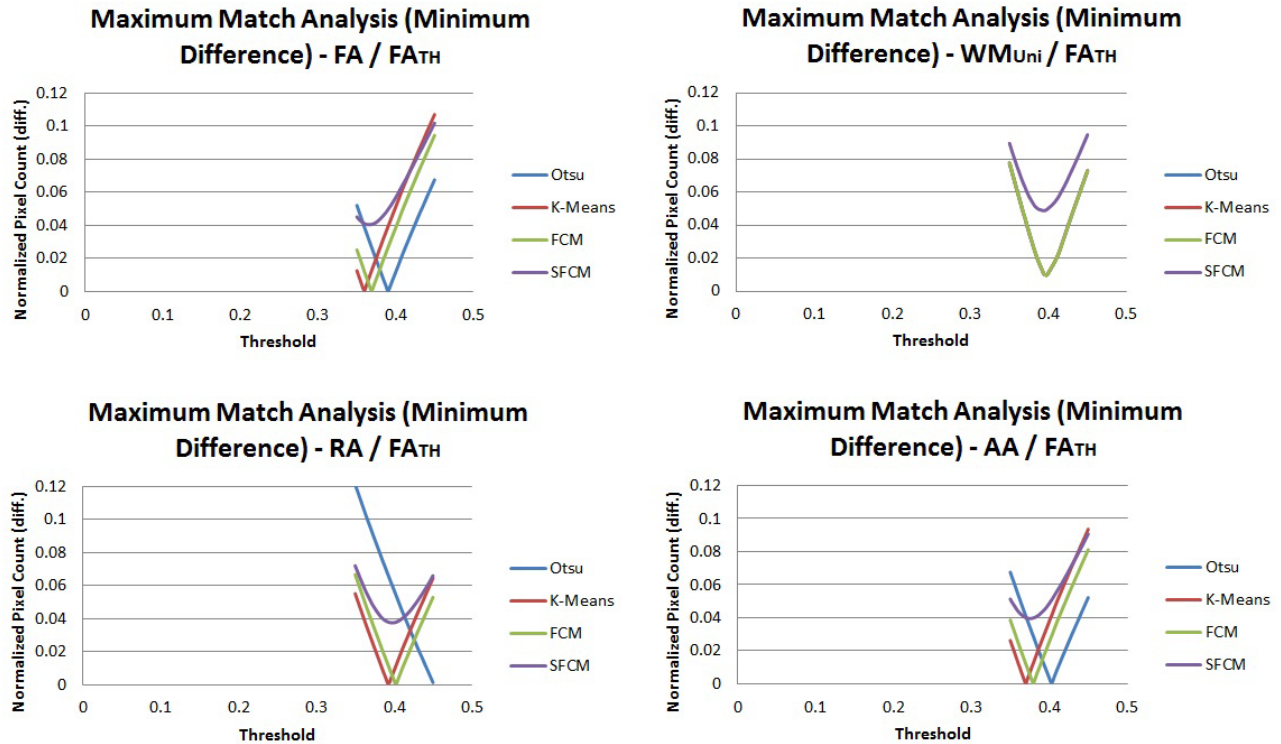
Figure 8. Maximum match analysis for WM segmentation using FA threshold clustering maps and some cluster maps generated using some clustering methods for different images.

universal because different regular segmentation settings are taken into consideration as different points of view for problem solution. The stability factor of unstable images is measured by RE analysis, where they give the smallest values compared to other images, which makes them closer to becoming clustering algorithm-independent. Clustering maps of unstable images produced from different clustering methods give similar threshold points in the histogram of FA (for WM/non-WM clustering) and similar threshold points in the histogram of MD (for CSF/non-CSF clustering) in the maximum match case; however, other SIs' clustering maps have ranges of values. This also verifies the stability of the unstable images. Improved results of the unstable method depend on some factors; the first factor is the selection of suitable input images where target tissues should be remarkable, the second factor is the suitable settings of the used clustering methods, and the last factor is the CM fusion function. In a previous study [14], DV was proved to provide good results for clustering CSF/non-CSF tissues with 3 clusters in the case of considering all foreground clusters to be CSF regions (tissue and background only); then:

$$F(CM_i) = \begin{cases} 1 & \text{for} \quad DV \, \forall \, CM_i\,(x,y) \neq 0 \\ CM_i & \text{else} \end{cases} \tag{6}$$

With this function, a slight difference in the modified CSF_{Uni} is obtained compared to the generic CSF_{Uni} (Figure 9); however, much better RE results are produced (Table 5).

Furthermore, improved quality for the modified WM_{Uni} compared to the generic WM_{Uni} (Figure 10) and better RE values (Table 6) can be obtained when the used function is determined by:

Table 1. The average of the mean and the SD of 5 human brains' RE analysis of different clustering methods for CSF/non-CSF clustering from different images.

	MD	DV	$\lambda 1$	$\lambda 2$	$\lambda 3$	CSF_{Uni}
RE_{AVG}	1.80 ±0.68	4.08 ±3.86	2.03 ±0.88	1.88 ±0.71	2.00 ±0.72	1.07 ±0.44

Table 2. The average of the mean and the SD of 5 human brains' RE analysis of different clustering methods for WM/non-WM clustering from different images.

	FA	RA	VR	AA	Cl	WM_{Uni}
RE_{AVG}	3.72 ±1.55	5.19 ±2.45	3.62 ±2.65	4.00 ±1.58	5.08 ±2.70	2.16 ±1.83

Table 3. The average of the mean and the SD of 5 human brains' threshold of maximum match analysis of different clustering methods for CSF/non-CSF clustering.

	MD	DV	$\lambda 1$	$\lambda 2$	$\lambda 3$	CSF_{Uni}
TH_{AVG}	0.30 ±0.012	0.30 ±0.034	0.32 ±0.012	0.30 ±0.012	0.28 ±0.014	0.29 ±0.002

Table 4. The average of the mean and the SD of 5 human brains' threshold of maximum match analysis of different clustering methods for WM/non-WM clustering.

	FA	RA	VR	AA	Cl	WM_{Uni}
TH_{AVG}	0.37 ±0.013	0.41 ±0.026	0.45 ±0.010	0.38 ±0.016	0.44 ±0.011	0.39 ±0.003

Table 5. Mean and SD of 5 human brains' RE analysis of different clustering methods in both the generic and the modified settings for CSF/non-CSF unistable images.

	Brain1	Brain2	Brain3	Brain4	Brain5	RE_{AVG}
Generic CSF_{Uni}	0.92 ±0.31	1.31 ±0.45	1.23 ±0.41	1.19 ±0.40	0.72 ±0.64	1.07 ±0.44
Modified CSF_{Uni}	0.56 ±0.48	0.77 ±0.63	0.70 ±0.57	0.67 ±0.55	0.63 ±0.51	0.67 ±0.55

Table 6. Mean and SD of 5 human brains' RE analysis of different clustering methods in both the original and the modified settings for WM/non-WM unistable images.

	Brain1	Brain2	Brain3	Brain4	Brain5	RE_{AVG}
Generic WM_{Uni}	1.86 ±1.50	2.20 ±1.84	2.23 ±1.95	2.13 ±1.85	2.40 ±2.00	2.16 ±1.83
Modified WM_{Uni}	1.48 ±1.59	1.98 ±1.73	1.89 ±1.63	1.83 ±1.59	1.67 ±1.76	1.77 ±1.66

$$f(CM_i) = \begin{cases} 1 - CM_i & \text{for} \quad VR \,\forall\, CM_i(x,y) \neq 0 \\ CM_i & \text{else} \end{cases} \tag{7}$$

Then:

$$F(CM_i) = f(CM_i)^2 + f(CM_i) \tag{8}$$

Finally, it is concluded that the unistable method might be a straightforward solution for the segmentation problem of medical images, where the segmentation process can be achieved using only one unistable image and any clustering method.
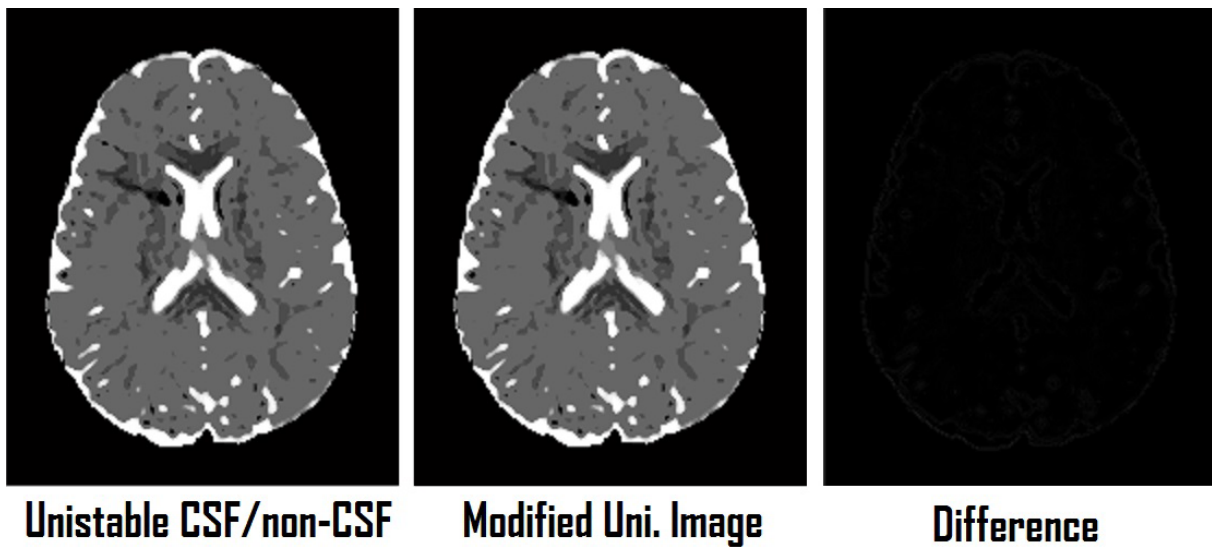
Figure 9. CSF/non-CSF unstable image with generic setting, modified CSF/non-CSF unstable image, and difference map between the two images.
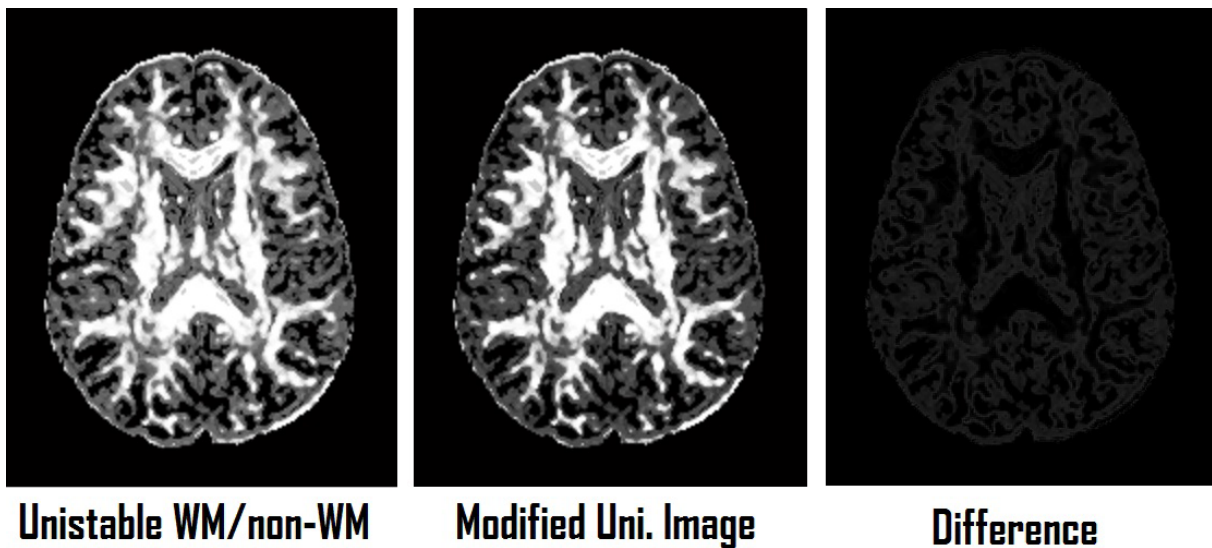

Figure 10. WM/non-WM unstable image with generic setting, modified WM/non-WM unstable image, and difference map between the two images.

Acknowledgment

References

[1] Mori S. Introduction to Diffusion Tensor Imaging. 1st ed. Oxford, UK: Elsevier, 2007.

[2] Liu T, Li H, Wong K, Tarokh A, Guo L, Wong S. Brain tissue segmentation based on DTI data. Neuroimage 2007; 38: 114-123.

[3] Zarei M, Johansen Berg H, Matthews PM. Diffusion tensor imaging and tractography in clinical neurosciences. Iranian Journal of Radiology 2003; 1: 45-52.

[4] Khotanlou H, Colliot O, Atif J, Bloch I. 3D brain tumor segmentation in MRI using fuzzy classification, symmetry analysis and spatially constrained deformable models. Fuzzy Set Syst 2009; 160: 1457-1473.

[5] Dubey RB, Hanmandlu M, Gupta SK, Gupta SK. The brain MR image segmentation techniques and use of diagnostic packages. Acad Radiol 2010; 17: 658-671.

[6] Sidaros A, Engberg AW, Sidaros K, Liptrot MG, Herning H, Petersen P, Paulson OB, Jernigan TL, Rostrup E. Diffusion tensor imaging during recovery from severe traumatic brain injury and relation to clinical outcome: a longitudinal study. Brain 2008; 131: 559-572.

[7] Holtmannspotter M, Peters N, Opherk C, Martin D, Herzog J, Bruckmann H, Samann P, Gschwendtner A, Dichgans M. Diffusion magnetic resonance histograms as a surrogate marker and predictor of disease progression in CADASIL: a two-year follow-up study. Stroke 2005; 36: 2559-2565.

[8] Albrecht J, Dellani PR, Muller MJ, Schermuly I, Beck M, Stoeter P, Gerhard A, Fellgiebel A. Voxel based analyses of diffusion tensor imaging in Fabry disease. J Neurol Neurosur Ps 2007; 78: 964-969.

[9] Concha L, Gross DW, Beaulieu C. Diffusion tensor tractography of the limbic system. Am J Neuroradiol 2005; 26: 2267-2274.

[10] Bomans M, Hohne KH, Kramer LH, Riemer M. 3-D segmentation of MR images of the head for 3-D display. IEEE T Med Imaging. 1990; 9: 177-183.

[11] Westbrook C, Roth CK, Talbot J. MRI in Practice. 4th ed. Oxford, UK: Wiley-Blackwell, 2011.

[12] Goldman LW. Principles of CT and CT technology. J Nucl Med Technol 2007; 35: 115-128.

[13] Portela NM, Cavalcanti G, Ren TI. Semi-supervised clustering for MR brain image segmentation. Expert Syst Appl 2014; 41: 1492-1497.

[14] El-Aff I. Human brain tissues segmentation based on DTI data. In: 11th International Conference on Information Science, Signal Processing and Their Applications; 2–5 July 2012; Montreal, Canada. New York, NY, USA: IEEE. pp. 876-881.

[15] Clarke LP, Velthuizen RP, Camacho MA. MRI Segmentation: methods and applications. Magn Reson Imaging 1995; 13: 343-368.

[16] Zhang Y, Brady M, Smith S. Segmentation of brain MR images through a hidden Markov random field model and the expectation-maximization algorithm. IEEE T Med Imaging 2001; 20: 45-57.

[17] Chen T, Huang TS. Region based hidden Markov random field model for brain MR image segmentation. International Journal of Computer, Electrical, Automation, Control and Information Engineering 2007; 1: 1129-1132.

[18] Perez P. Markov random fields and images. CWI Quarterly 1998; 11: 413-437.

[19] Demirkaya O, Asyali MK, Sahoo PK. Image Processing with MATLAB: Application in Medicine and Biology. Boca Raton, FL, USA: CRC Press, 2009.

[20] Otsu N. A threshold selection method from gray-level histograms. IEEE T Syst Man Cyb 1979; 9: 62-66.

[21] Wagsta K, Cardie C, Rogers S, Schroedl S. Constrained K-means clustering with background knowledge. In: Proceedings of the Eighteenth International Conference on Machine Learning; 28 June–1 July 2001; Williamstown, MA, USA. Burlington, MA, USA: Morgan Kaufmann. pp. 577-584.

[22] Dempster AP, Laird NM, Rubin DB. Maximum likelihood from incomplete data via the EM algorithm. J R Stat Soc 1977; 39: 1-38.

[23] Wen Y, He L, Von Deneen KM, Lu Y. Brain tissue classification based on DTI using an improved fuzzy C-means algorithm with spatial constraints. Magn Reson Imaging 2013; 31: 1623-1630.

[24] Freitas P, Rittner L, Appenzeller S, Lotufo R. Watershed-based segmentation of the midsagittal section of the corpus callosum in diffusion MRI. In: 24th SIBGRAPI Conference on Graphics, Patterns and Images; 28–31 August 2011; Alagoas, Brazil. pp. 274-281.

[25] Song Z, Tustison N, Avants B, Gee JC. Integrated graph cuts for brain MRI segmentation. In: 9th International Conference in Medical Image Computing and Computer-Assisted Intervention; 1–6 October 2006; Copenhagen, Denmark. Berlin, Germany: Springer. pp. 831-838.

[26] Awate PS, Tasdizen T, Foster N, Whitaker RT. Adaptive Markov modeling for mutual-information-based, unsupervised MRI brain-tissue classification. Med Image Anal 2006; 10: 726-739.

[27] Li H, Liu T, Young G, Guo L, Wong ST. Brain tissue segmentation based on DWI/DTI data. In: 3rd IEEE International Symposium on Biomedical Imaging; 6–9 April 2006; Arlington, VA, USA. New York, NY, USA: IEEE. pp. 57-60.

[28] Mortamet B, Zeng D, Gerig G, Prastawa M, Bullitt E. Effects of healthy aging measured by intracranial compartment volumes using a designed MR brain database. In: 8th International Conference on Medical Image Computing and Computer-Assisted Intervention; 26–29 October 2005; Palm Springs, CA, USA. Berlin, Germany: Springer. pp. 383-391.

[29] Gur RC, Gunning-Dixon F, Bilker WB, Gur RE. Sex differences in temporo-limbic and frontal brain volumes of healthy adults. Cereb Cortex 2002; 12: 998-1003.

[30] Basser PJ, Mattiello J, LeBihan D. MR diffusion tensor spectroscopy and imaging. Biophys J 1994; 66: 259-267.

[31] Basser PJ, Pierpaoli C. Microstructural and physiological features of tissues elucidated by quantitative-diffusion-tensor MRI. J Magn Reson 1996; 111: 209-219.

[32] Vilanova A, Zhang S, Kindlmann G, Laidlaw D. An introduction to visualization of diffusion tensor imaging and its applications. In: Weickert J, Hagen H, editors. Visualization and Processing of Tensor Fields. Berlin, Germany: Springer, 2005. pp. 121-153.

[33] El-Aff I. Extraction of human heart conduction network from diffusion tensor MRI. In: Bipmed2010; 17–19 February 2010; Innsbruck, Austria. Calgary, Canada: ACTA Press. p. 680-051.

[34] Arlot S, Celisse A. A survey of cross-validation procedures for model selection. Stat Surv J 2010; 4: 40-79.

[35] Seehaus A, Roebroeck A, Bastiani M, Fonseca L, Bratzke H, Lori N, Vilanova A, Goebel R, Galuske R. Histological validation of high-resolution DTI in human post mortem tissue. Front Neuroanat 2015; 9: 98.